The Astrophysical Journal, 703:2138–2151, 2009 October 1 doi:10.1088/0004-637X/703/2/2138


# QUANTIFYING THE ANISOTROPY AND SOLAR CYCLE DEPENDENCE OF "$1/f$" SOLAR WIND FLUCTUATIONS OBSERVED BY *ADVANCED COMPOSITION EXPLORER*

R. M. Nicol[1], S. C. Chapman[1], and R. O. Dendy[1,2]
[1] Centre for Fusion, Space and Astrophysics, Department of Physics, University of Warwick, Coventry, CV4 7AL, UK; R.M.Nicol@warwick.ac.uk
[2] UKAEA Culham Division, Culham Science Centre, Abingdon, Oxfordshire, OX14 3DB, UK
*Received 2009 June 15; accepted 2009 August 25; published 2009 September 16*

## ABSTRACT

The power spectrum of the evolving solar wind shows evidence of a spectral break between an inertial range (IR) of turbulent fluctuations at higher frequencies and a "$1/f$" like region at lower frequencies. In the ecliptic plane at $\sim$1 AU, this break occurs approximately at timescales of a few hours and is observed in the power spectra of components of velocity and magnetic field. The "$1/f$" energy range is of more direct coronal origin than the IR, and carries signatures of the complex magnetic field structure of the solar corona, and of footpoint stirring in the solar photosphere. To quantify the scaling properties we use generic statistical methods such as generalized structure functions and probability density functions (PDFs), focusing on solar cycle dependence and on anisotropy with respect to the background magnetic field. We present structure function analysis of magnetic and velocity field fluctuations, using a novel technique to decompose the fluctuations into directions parallel and perpendicular to the mean local background magnetic field. Whilst the magnetic field is close to "$1/f$," we show that the velocity field is "$1/f^{\alpha}$" with $\alpha \neq 1$. For the velocity, the value of $\alpha$ varies between parallel and perpendicular fluctuations and with the solar cycle. There is also variation in $\alpha$ with solar wind speed. We have examined the PDFs in the fast, quiet solar wind and intriguingly, whilst parallel and perpendicular are distinct, both the $\boldsymbol{B}$ field and velocity show the same PDF of their perpendicular fluctuations, which is close to gamma or inverse Gumbel. These results point to distinct physical processes in the corona and to their mapping out into the solar wind. The scaling exponents obtained constrain the models for these processes.

*Key words:* magnetic fields – methods: statistical – solar wind – turbulence

*Online-only material:* color figures

## 1. INTRODUCTION

The solar corona expands non-uniformly into space as a supersonic plasma outflow known as the solar wind (Parker 1958). The solar wind carries signatures of coronal dynamics as well as locally generated turbulent phenomena, which span a broad range of scales.

In situ spacecraft observations of fluctuations in solar wind parameters such as velocity and magnetic field (for example, Ruzmaikin et al. 1993 in the ecliptic plane and Horbury et al. 1995 in polar flows) typically reveal an inertial range (IR) of turbulence with a "5/3" inverse power-law scaling at high frequencies and a flatter "$1/f$"-like scaling range at lower frequencies (Matthaeus & Goldstein 1986). The breakpoint between these two ranges is seen to evolve radially (Bavassano et al. 1982; Horbury et al. 1996) with the IR extending to lower frequencies with increasing radial distance, suggesting a turbulent energy cascade in the solar wind. The solar wind also has a background magnetic field and is therefore a highly anisotropic plasma environment (Shebalin et al. 1983; Oughton et al. 1994). The strength of this background field relative to the amplitude of the fluctuations determines whether the turbulence is "strong," i.e., the amplitude of fluctuations is comparable to that of the background magnetic field (Sridhar & Goldreich 1994; Goldreich & Sridhar 1995) or "weak," i.e., the background magnetic field is dominant (Ng & Bhattacharjee 1997; Galtier et al. 2000). This IR has been extensively studied using time series analysis techniques including power spectra (Marsch & Tu 1990a), probability density functions (PDFs; Marsch & Tu 1997; Padhye et al. 2001; Bruno et al. 2004) and generalized structure functions (GSFs; e.g., Horbury & Balogh 1997; Hnat et al. 2005; Sorriso-Valvo et al. 2007; Chapman & Hnat 2007; Nicol et al. 2008).

In this paper, we focus on the low frequency "$1/f^{\alpha}$" range, where the observed $\alpha \sim 1$ for magnetic field fluctuations, which is ubiquitous in the solar wind and seen at all latitudes and radial distances. It is dominated by signatures of coronal origin (see Matthaeus & Goldstein 1986), unlike the turbulence seen at higher frequency, which is locally evolving. Indeed, at lower frequencies, the dominant process may be transport, however, it is still possible that local scaling could arise, for example, from coronal processes advected outward by the expanding solar wind. Multifractal scaling can arise from a variety of processes with non-Gaussian statistics Sornette (2004), of which in situ generated turbulence is just a subset. The location of the spectral breakpoint between the inertial and "$1/f$" ranges depends on latitude and radial distance, but it is always possible to see "$1/f$" scaling at low frequencies. The power spectral density (PSD) of the "$1/f$" range in the interplanetary magnetic field has been extensively studied by Matthaeus & Goldstein (1986) and at 1 AU in the magnitude of the solar wind bulk velocity $\boldsymbol{v}$ and magnetic field $\boldsymbol{B}$ by Burlaga & Forman (2002). There is also an extensive body of work on the Gaussian and non-Gaussian properties of PDFs of fluctuations in solar wind parameters at these very large scales (Marsch & Tu 1997; Burlaga & Forman 2002; Sorriso-Valvo et al. 2004; Bavassano et al. 2005) and over a wide range of heliospheric radii. Burlaga & Forman (2002) used large-scale velocity fluctuations at 1 AU on timescales of 1 hr to a year to quantify the standard deviation, kurtosis, and skewness of PDFs over these scales. Studies of the "$1/f$" range in the solar wind thus provide a unique perspective on the physics of coronal processes over the solar cycle. For the first time we consider components of $\boldsymbol{v}$ and $\boldsymbol{B}$ defined relative to the local magnetic field, and we systematically distinguish between intervals of fast and slow solar wind at solar maximum and minimum. Here we will focus on the anisotropy of the fluctuations by using a novel decomposition technique, and will take advantage of the long time series available from the *Advanced Composition Explorer* (*ACE*) spacecraft to compare not only fast and slow solar wind streams but also periods of minimum and maximum solar activity.

In the IR, vector quantities such as in situ velocity and magnetic field can be resolved for components both parallel and perpendicular with respect to the background magnetic field $\boldsymbol{B}$. The duration of the timescale over which the background field is computed is important and both large-scale $\boldsymbol{B}$ (Matthaeus et al. 1990) and average local $\boldsymbol{B}$ as a function of the scale of the fluctuations (Chapman & Hnat 2007; Horbury et al. 2008) have been considered in the context of IR turbulence. In terms of quantifying scaling, these approaches are generic and the focus of the present paper is to incorporate these ideas in statistical studies of the "$1/f$" range. In this region, we are not straightforwardly concerned with in situ turbulence, rather with some other scaling signal which is a consequence of a combination of remote processes at the corona and convection as well as active mixing. The natural coordinate set is therefore far from clear; here, we explore the idea that the background magnetic field orders processes such as magnetohydrodynamics (MHD) turbulent mixing and convection. We will test whether the statistical properties of the fluctuations in $\boldsymbol{v}$ and $\boldsymbol{B}$ are related: specifically, whether they show the same PDF and scaling exponents. We need to select a single coordinate system in which to project both $\boldsymbol{v}$ and $\boldsymbol{B}$ fluctuations to facilitate comparison and here we choose this to be oriented with respect to the local background $\boldsymbol{B}$ field. The observed scaling would also be anticipated to depend quantitatively on solar cycle and to differ between fast ($\sim$750 km s$^{-1}$) or slow ($\sim$350 km s$^{-1}$) solar wind streams. High-speed flows originate in coronal holes (Krieger et al. 1973), whereas low-speed flows arise from dense coronal streamers (Gosling et al. 1981), while solar rotation causes high- and low-speed flows to interact at low latitudes. We will perform generalized structure function analysis (GSF; Sornette 2004) on data sets spanning these intervals in order to quantify the scaling properties of the magnetic and velocity field fluctuations both parallel and perpendicular to the background magnetic field $\boldsymbol{B}$.

The location of the spectral breakpoint between the inertial and "$1/f$" ranges differs in fast and slow streams (Horbury et al. 2005; Bruno & Carbone 2005), presumably because at a given heliocentric distance the turbulence in the slow solar wind has had more time to develop than in the fast solar wind. Furthermore, the crossover between IR and "$1/f$" is much clearer in fast than in slow solar wind. Here, we will see that projecting velocity and magnetic field parallel and perpendicular to $\boldsymbol{B}$ provides a clear indicator of where this crossover occurs. We compare the position of this breakpoint in fast and slow solar wind streams and at periods of maximum and minimum solar activity. We first see that the PSDs of the vector components of the velocity $\boldsymbol{v}$ and magnetic field $\boldsymbol{B}$ suggest anisotropy in the "$1/f$" range. We then decompose $\boldsymbol{v}$ and $\boldsymbol{B}$ into parallel and perpendicular fluctuations with respect to the local background magnetic field $\boldsymbol{B}$. For the simple case of quiet fast solar wind, we compare the PDFs of the fluctuations to see which components may or may not share the same underlying generating process. For completeness, we also consider the PDF for the density fluctuations $\delta\rho$. We compare the GSFs for fast and slow solar wind at solar maximum and minimum. Finally, using the GSFs, we obtain values for the scaling exponents in the "$1/f$" range and find that these are clearly distinct for $\delta v_{\parallel,\perp}$ and $\delta b_{\parallel,\perp}$.

## 2. THE DATA SETS

The *ACE* spacecraft (Stone et al. 1998) orbits the Lagrangian point sunward of the earth ($\sim$1 AU). For the present analysis we study plasma parameters (magnetic field $\boldsymbol{B}$ and velocity $\boldsymbol{v}$) averaged over 64 s from the MAG/SWEPAM teams (Smith et al. 1998; McComas et al. 1998): for the year 2007, representative of a period of minimum solar activity; and for the year 2000, which was a period of maximum solar activity. This provides data sets of $\sim 4.8 \times 10^5$ samples per year. In order to separate fast and slow solar wind behavior yet still preserve a data set with sufficient points to perform GSF to explore the "$1/f$" dynamic frequency range, we divide the data set into intervals ($\geqslant$ 6000 points or 4.5 days) of fast and slow streams, where the cutoff between fast and slow is taken at 450 km s$^{-1}$ (e.g., Horbury et al. 2005). These intervals then form one long fast solar wind data set of $\sim 7.4 \times 10^4$ points, and one long slow solar wind data set of $\sim 1.4 \times 10^5$ points for the year 2007 and a fast data set of $\sim 4.1 \times 10^4$ points and a slow data set of $\sim 1.1 \times 10^5$ points for the year 2000. To evaluate spectral properties, we apply Fourier techniques to the original continuous intervals of fast and slow solar wind. When we perform statistical analysis using the PDFs of fluctuations in Section 3, each data set is treated as a single ensemble. As we preserve the time indicators for the data, the pairs of data points are always drawn from within continuous intervals of fast or slow streams.

We first provide an overview of the "$1/f$" range of these data intervals by plotting the PSD $F(f)$ of the components of $\boldsymbol{v}$ and $\boldsymbol{B}$ in the $RTN$ coordinate system, where $R$ is the sun-spacecraft axis, $T$ is the cross-product of $R$ with the solar rotation axis, and $N$ is the cross-product of $R$ with $T$. Generally, for a signal $x(t)$ of length $N$, the power spectrum $F(f)$ from the fast Fourier transform (FFT) to frequency space is given by

$$F(f) = \frac{1}{N} \left| \sum_{t=1}^{N} x(t) e^{-2i\pi(t-1)(f-1)/N} \right|^2 \qquad (1)$$

for a range of frequencies $f = \frac{n}{N f_s}$ where $n = [0 : N/2]$ and $f_s$ is the sampling frequency. We take our original intervals of fast and slow solar wind and truncate (or cut) them such that they all have the same length of 6000 data points. Each interval is then split up into windows of $2^{12} = 4096$ points with a 50% overlap on the previous window. A Hamming window is applied to each of these sub-intervals and the FFT is computed. An average is then taken of these sub-interval FFTs to obtain the power spectrum for each interval. The power spectra for all intervals are then averaged to obtain the PSDs for fast and slow solar wind at both solar maximum and minimum. At lower frequencies, the magnetic field power spectrum $F(f) \sim f^{\alpha}$ shows a spectral slope $\alpha \sim -1$. Plotting $F(f)/f^{\alpha}$, $\alpha = -1$ should therefore give a horizontal line (on average). These plots are known as compensated power spectra and are shown for the various solar wind conditions in Figure 1. Figure 1 covers the expected region of transition in the spectral index of $\boldsymbol{v}$ and $\boldsymbol{B}$ between the IR and "$1/f$" frequency ranges. However it is difficult to tell precisely whether, for example, the PSD behavior between $10^{-5}$ Hz and $10^{-4}$ Hz really is "$1/f^{\alpha}$, $\alpha = 1$," particularly in the slow solar wind. It also evident from Figure 1 that in some cases in the "$1/f^{\alpha}$" range $\alpha$ varies with the solar cycle and with

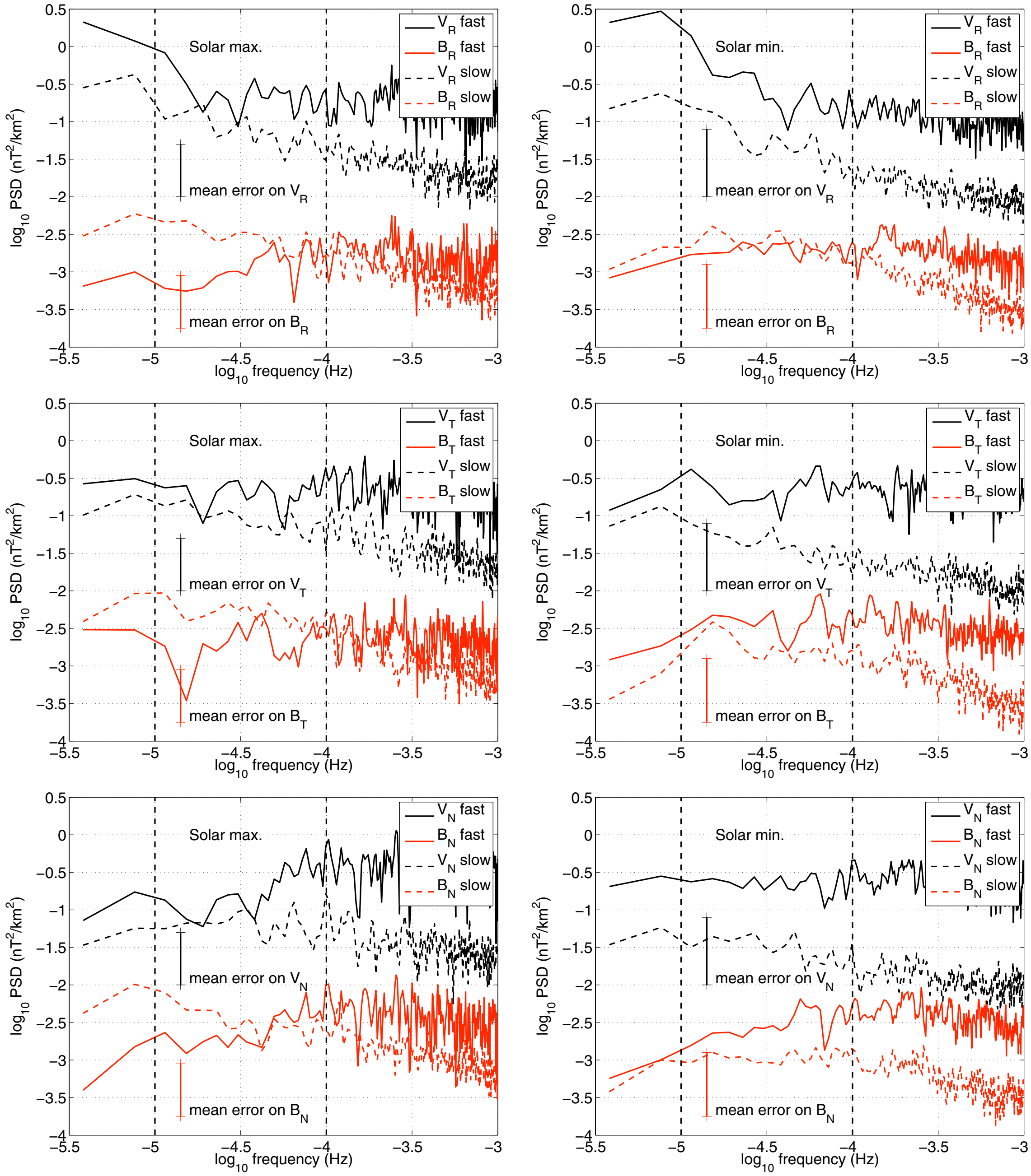


**Figure 1.** Compensated PSD $F(f)/f^{\alpha}$, $\alpha = -1$ for velocity and magnetic field fluctuation components in the $RTN$ coordinate system for the frequency range $10^{-5.5}$ to $10^{-3}$Hz. Results for the fast (continuous line) and slow (dashed line) are displayed separately. The dotted vertical lines delimit the frequency range $10^{-5}$ to $10^{-4}$Hz; this is expected to lie within the "$1/f$" range, with the breakpoint between the inertial and "$1/f$" ranges $\sim 10^{-4}$ Hz (Marsch & Tu 1990b; Horbury et al. 1996). The three panels on the left-hand side are for solar maximum, while the right-hand side is solar minimum. The errors are found by considering one standard deviation of the data sets over which the averages are taken.

(A color version of this figure is available in the online journal.)

solar wind speed, and that for both $\boldsymbol{v}$ and $\boldsymbol{B}$ the $\alpha$ can vary from one component to another, and between $\boldsymbol{v}$ and $\boldsymbol{B}$. This implies anisotropy in the fluctuations and distinct scaling between $\boldsymbol{v}$ and $\boldsymbol{B}$.

From a statistical point of view, let us now characterize this anisotropy by decomposing the velocity (or magnetic) field fluctuations into parallel and perpendicular components relative to the background magnetic field. We adopt the Taylor hypothesis (Taylor 1938) to relate spatial and temporal scales and fluctuations over a time lag $\tau$ in the velocity (or magnetic field) vector components, defined as $\delta\boldsymbol{v}(t,\tau) = \boldsymbol{v}(t+\tau) - \boldsymbol{v}(t)$. A vector average for the magnetic field direction $\hat{\boldsymbol{b}}(t,\tau) = \overline{\boldsymbol{B}}/|\overline{\boldsymbol{B}}|$ is formed from a vector sum $\overline{\boldsymbol{B}}(t)$ of all the observed vector $\boldsymbol{B}$ values between $t - \tau/2$ and $t + 3\tau/2$. It follows that in computing fluctuations over $\tau$, the background field is averaged over $\tau' = 2\tau$, which then defines the minimum (Nyquist) interval necessary to capture wavelike fluctuations (Chapman & Hnat 2007). Using this definition of $\hat{\boldsymbol{b}}$, the inner product

$$\delta v_{\parallel} = \delta\boldsymbol{v} \cdot \hat{\boldsymbol{b}} = \delta v_R \hat{b}_R + \delta v_T \hat{b}_T + \delta v_N \hat{b}_N \tag{2}$$

vanishes for fluctuations which generate a velocity displacement that is purely perpendicular to the background magnetic field $\overline{\boldsymbol{B}}$ as defined. The perpendicular fluctuation amplitude is then obtained from

$$\delta v_{\perp} = \sqrt{\delta \boldsymbol{v} \cdot \delta \boldsymbol{v} - (\delta \boldsymbol{v} \cdot \hat{\boldsymbol{b}})^2}. \tag{3}$$

We use these definitions to construct differenced time series $\delta v_{\perp}(t, \tau)$, $\delta b_{\perp}(t, \tau)$, $\delta v_{\parallel}(t, \tau)$ and $\delta b_{\parallel}(t, \tau)$ over a range of $\tau$ intervals within the "$1/f$" range, that is $\tau$ from a few hours up to a day.

We note that our definition of the perpendicular component is a scalar unsigned quantity, this can be thought of as an angle-averaged component in the plane perpendicular to the background field $\overline{\boldsymbol{B}}$. This relies on the assumption of isotropy in this plane. In order to test this we decompose the perpendicular fluctuations into two signed orthogonal components and compare their PDFs. We first define two orthogonal unit vectors in the perpendicular plane as

$$\hat{\boldsymbol{e}}_{\perp,\mathbf{1}} = \frac{\hat{\boldsymbol{b}} \times \langle \boldsymbol{v} \rangle}{|\hat{\boldsymbol{b}} \times \langle \boldsymbol{v} \rangle|} \tag{4}$$

and

$$\hat{\boldsymbol{e}}_{\perp,\mathbf{2}} = \frac{\hat{\boldsymbol{b}} \times \hat{\boldsymbol{e}}_{\perp,\mathbf{1}}}{|\hat{\boldsymbol{b}} \times \hat{\boldsymbol{e}}_{\perp,\mathbf{1}}|} = \frac{\hat{\boldsymbol{b}} \times (\hat{\boldsymbol{b}} \times \langle \boldsymbol{v} \rangle)}{|\hat{\boldsymbol{b}} \times (\hat{\boldsymbol{b}} \times \langle \boldsymbol{v} \rangle)|}, \tag{5}$$

where $\langle \boldsymbol{v} \rangle$ is the mean velocity over the total considered time period and $\hat{\boldsymbol{b}}$ is a unit vector in the direction of the local background magnetic field as defined previously. Velocity fluctuations along these axis are then formed by the following inner products:

$$\delta v_{\perp,1} = \delta \boldsymbol{v} \cdot \hat{\boldsymbol{e}}_{\perp,\mathbf{1}} \tag{6}$$

and

$$\delta v_{\perp,2} = \delta \boldsymbol{v} \cdot \hat{\boldsymbol{e}}_{\perp,\mathbf{2}}. \tag{7}$$

These quantities are computed for the entire $\tau$ range examined and normalized by their mean and standard deviation in order to be compared. Figure 2 shows that any anisotropy present in the perpendicular plane is very weak, justifying our assumption of isotropy and our use of a scalar, unsigned perpendicular fluctuation as defined by Equation (3). The fluctuations depart from Gaussian at large values (the tails). We compute the excess kurtosis of the fluctuations to estimate the extent of this departure from Gaussian. The excess kurtosis is defined as $\langle \delta v^4_{\perp,1\&2} \rangle / \langle \delta v^2_{\perp,1\&2} \rangle^2 - 3$. For a normal distribution it is therefore equal to zero. We find values of kurtosis in the range $\sim$[0.27–0.72] for both perpendicular velocity components for the "$1/f$" range $\tau = 320$–1003 minutes. The values are small compared to some solar wind kurtosis measurements, which can reach $\sim$10 (e.g., Feynman & Ruzmaikin 1994), nevertheless they confirm the non-Gaussian nature of the PDFs.

## 3. PDF ANALYSIS

We first examine the PDFs of these fluctuations and explore their possible functional forms. For a self-affine process, knowledge of the functional form of the PDF, and of the Hurst exponent $H$, is sufficient in principle to build a stochastic differential equation model for the process (e.g., Sornette 2004; Chapman et al. 2005; Kiyani et al. 2007). To compare their functional form, the PDFs can be renormalized using (e.g., Greenhough et al. 2002)

$$P[(y - \langle y \rangle)] = \sigma^{-1} P[\sigma^{-1}(y - \langle y \rangle)], \tag{8}$$

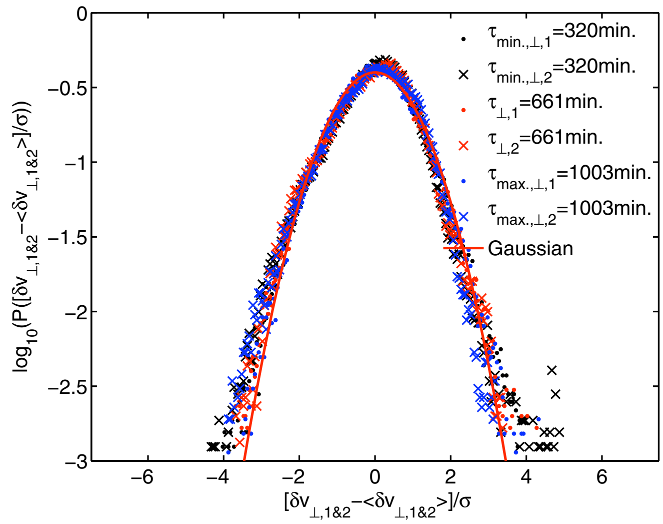


**Figure 2.** Perpendicular velocity fluctuations $\delta v_{\perp,1}$ ("·") and $\delta v_{\perp,2}$ ("×") in the fast solar wind at solar minimum for the "$1/f$" range. The normalized PDFs are plotted on semilog $y$ axes. For clarity, plots for only three representative values of $\tau$ are shown for each component, whereas the fitted curve is computed using all the $\tau$ intervals between 320 and 1003 minutes. A Gaussian fit to the normalized PDF curves for both $\delta v_{\perp,1}$ and $\delta v_{\perp,2}$ is shown.

(A color version of this figure is available in the online journal.)

where $\langle \cdots \rangle$ denotes the ensemble mean and $\sigma$ is the standard deviation of the distribution. From a statistical point of view, where fluctuations arise from a single physical process, rescaling of PDFs using Equation (8) leads to the "collapse" of the PDFs for the different $\tau$ onto a single function that characterizes the underlying process (e.g., Greenhough et al. 2002; Dudson et al. 2005; Dendy & Chapman 2006; Dewhurst et al. 2008; Hnat et al. 2008). Let us apply this technique to parallel and perpendicular velocity and magnetic field fluctuations in the fast solar wind at solar minimum. Figure 3 shows that the PDFs for the $\delta v_{\parallel}$ and $\delta v_{\perp}$ components each collapse onto single curves that are distinct from each other. The PDF for $\delta v_{\parallel}$ is asymmetric about $\delta v_{\parallel} = 0$, and we have investigated this asymmetry by sorting the fluctuations with respect to the sign of $\delta v_R$ into $\delta v^+_{\parallel}$ and $\delta v^-_{\parallel}$. The resulting GSFs and scaling exponents display the same fractal characteristics as $\delta v_{\parallel}$, implying that $\delta v^+_{\parallel}$ and $\delta v^-_{\parallel}$ arise from the same physical process. Figure 4 shows that the PDFs for $\delta b_{\parallel}$ and $\delta b_{\perp}$ each collapse onto single curves that are distinct from each other. The curve for $\delta b_{\parallel}$ is distinct from that for $\delta v_{\parallel}$ and the PDF has stretched exponential tails, which implies that these fluctuations may originate in multiplicative or fractionating process (Frisch & Sornette 1997). The curves for $\delta b_{\perp}$ and $\delta v_{\perp}$ look remarkably similar and we will explore this later. The functional forms of these distributions are investigated in Figure 5. A Gaussian distribution (Wadsworth 1997)

$$f(x|\mu, \sigma) = \frac{1}{\sigma\sqrt{2\pi}} e^{\frac{-(x-\mu)^2}{2\sigma^2}} \tag{9}$$

approximately fits the normalized PDFs of the $\delta v_{\parallel}$ fluctuations in the "$1/f$" range shown in Figure 3 with the following fitting parameters and 95% confidence bounds: $\mu = 0 \pm 0.003$ (mean) and $\sigma = 1 \pm 0.002$ (standard deviation). Note that since we normalized the curves to $\mu$ and $\sigma$, an exact fit would have been $\mu = 0$ and $\sigma = 1$ here. In contrast, the normalized PDFs of the $\delta v_{\perp}$ fluctuations in the "$1/f$" range also shown in Figure 3 are clearly not Gaussian. Here they are fitted with two different heavy-tailed distributions: first, we take the inverse Gumbel

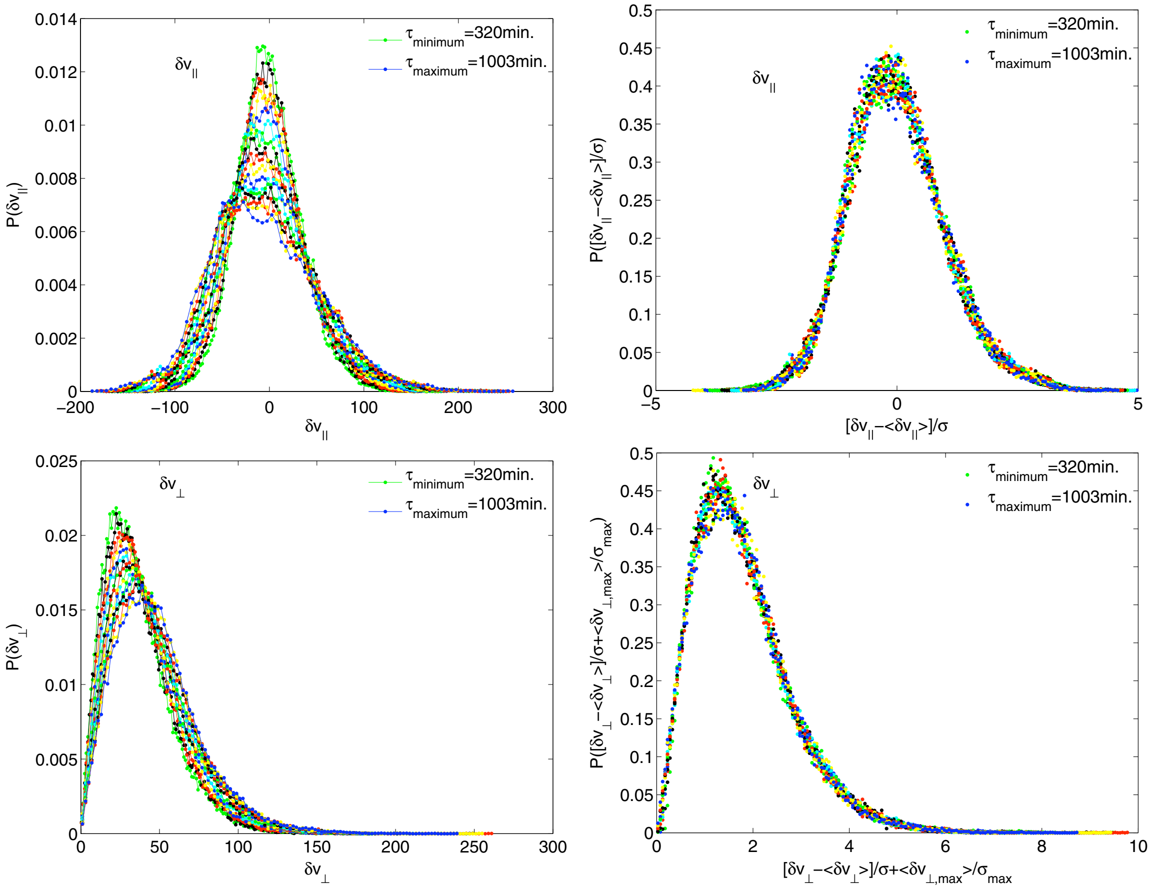


**Figure 3.** Parallel (upper) and perpendicular (lower) velocity fluctuations $\delta v_{\parallel,\perp}$ in the fast solar wind at solar minimum for the "$1/f$" range. The left panels show the PDFs of raw fluctuations sampled across intervals $\tau$ between 320 and 1003 minutes. The right panels show the same curves normalized using Equation (8).

(A color version of this figure is available in the online journal.)

distribution given by

$$f(x|k,\mu,\sigma) = \frac{1}{\sigma}\exp\left(-\exp\left(-\frac{(\mathrm{x}-\mu)}{\sigma}\right) - \frac{(\mathrm{x}-\mu)}{\sigma}\right). \quad (10)$$

This distribution corresponds to a maximum extreme value distribution or the limiting distribution of samples obtained by repeatedly selecting the maximum from an ensemble of events, which in turn, have a distribution with finite variance, e.g., Gaussian or exponential (Sornette 2004). Second, a lognormal distribution (Wadsworth 1997) defined by

$$f(x|\mu,\sigma) = \frac{1}{x\sigma\sqrt{2\pi}} e^{\frac{-(\ln x-\mu)^2}{2\sigma^2}} \quad (11)$$

is fitted. It can be seen from Figure 5 that the inverse Gumbel gives a good fit to the PDF of the $\delta v_\perp$ fluctuations.

Turning to the magnetic field, Figure 5 shows that, unlike $\delta v_\parallel$, for $\delta b_\parallel$ there is a strong departure from the Gaussian distribution in the tails of the PDF, which are closer to stretched exponential, reminiscent of turbulence. The PDFs of the $\delta b_\perp$ fluctuations in the "$1/f$" range are fitted with the same two heavy-tailed distributions as $\delta v_\perp$. Table 1 summarizes the fitting parameters for the different heavy tailed distributions for both $\delta v_\perp$ and $\delta b_\perp$.

There is little difference between the raw and collapsed PDFs, as $\delta b_{\parallel,\perp}$ is closer to "$1/f$" scaling.

As we have seen, $\delta b_\perp$ and $\delta v_\perp$ appear to be strongly similar in their statistics and Figure 6 overlays the normalized PDFs for $\delta b_\perp$ and $\delta v_\perp$ in the fast quiet solar wind. We see that they are almost identical. A possible interpretation is that both sets of fluctuations have the same physical process at their origin. It was also found that a gamma distribution (Wadsworth 1997) and (Graves et al. 2002, for example), was a good fit to the perpendicular fluctuations in the velocity and magnetic fields.

For completeness, we also examine the ion density fluctuations $\delta\rho$ in the fast quiet solar wind. From Matthaeus et al. (2007), one might expect these to show similar scaling behavior to the $\delta b_{\parallel,\perp}$ fluctuations, however in Figure 7 we see that this is not the case. The density PDFs have very sharp peaks with extended tails and are asymmetric. The rescaling collapse works well at the center of the PDFs, but not toward the tails.

**Table 1**
Fitting Parameters Obtained from Maximum Likelihood Estimates

| | | | | |
|---|---|---|---|---|
| Gumbel Parameters | | | | |
| | $\mu$ | $\pm$ | $\sigma$ | $\pm$ |
| $\delta v_\perp$ | 1.324 | 0.002 | 0.764 | 0.001 |
| $\delta b_\perp$ | 1.325 | 0.002 | 0.770 | 0.001 |
| Lognormal Parameters | | | | |
| | $\mu$ | $\pm$ | $\sigma$ | $\pm$ |
| $\delta v_\perp$ | 0.410 | 0.001 | 0.625 | 0.001 |
| $\delta b_\perp$ | 0.406 | 0.001 | 0.633 | 0.001 |

**Note.** Fitting parameters obtained from maximum likelihood estimates for the Gumbel and lognormal distributions for $\delta v_\perp$ and $\delta b_\perp$ in the fast solar wind at solar minimum.

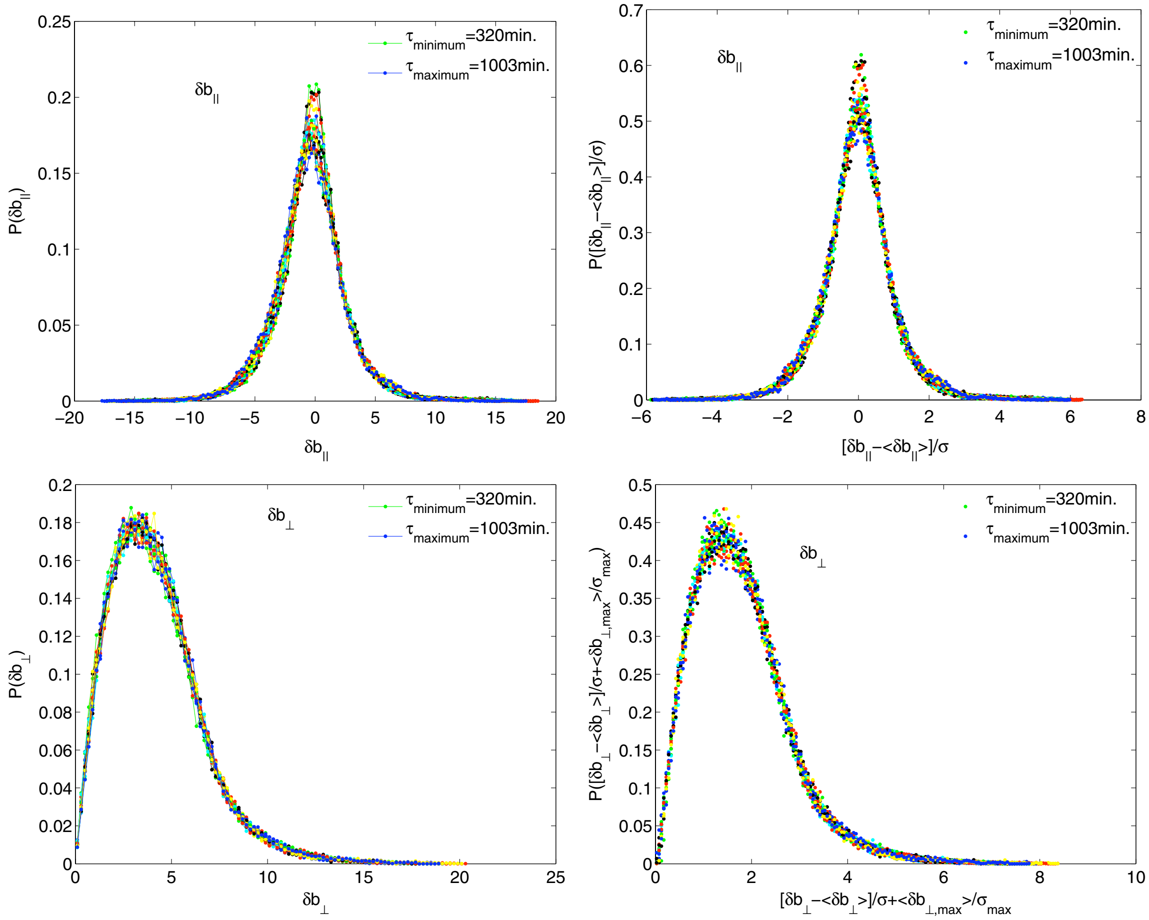


**Figure 4.** Parallel (upper) and perpendicular (lower) magnetic field fluctuations $\delta b_{\|,\perp}$ in the fast solar wind at solar minimum for the "$1/f$" range. The left panels show the PDFs of raw fluctuations sampled across intervals $\tau$ between 320 and 1003 minutes. The right panels show the same curves normalized using Equation (8). (A color version of this figure is available in the online journal.)

To conclude this section, let us summarize our analysis of the PDFs of fluctuations in the fast quiet solar wind.

1. Figures 3 and 4 (right-hand sides) show scaling collapse for $\delta v_{\|,\perp}$ and $\delta b_{\|,\perp}$.
2. Figure 5 (left-hand side) shows that $\delta v_{\|}$ and $\delta b_{\|}$ are distinct. This is manifest in both a different functional form of the rescaled PDFs and different scaling of the moments.
3. $\delta b_{\|}$ is nearly symmetric and has stretched exponential tails, consistent with a multiplicative process, whereas $\delta v_{\|}$ is more asymmetric and is close to Gaussian.
4. Figure 6 shows that $\delta v_{\perp}$ and $\delta b_{\perp}$ have the same PDF functional form and are reasonably well fitted by the gamma and Gumbel distributions with similar fitting parameters, suggesting a common source for the fluctuations.

## 4. GSF ANALYSIS FOR COMPARISON OF QUIET FAST AND SLOW STREAMS

Scaling can be quantified by computing the GSFs of the fluctuations, $\langle|\delta y_\tau|^m\rangle$, where $\langle\cdots\rangle$ denotes ensemble averaging, $m$ is the order of the moment and $\delta y_\tau = y(t+\tau) - y(t)$ is the fluctuation in a signal $y(t)$ over a time $\tau$. Assuming weak stationarity and a degree of self-similarity, GSFs can be related to the scale $\tau$ of the fluctuation by a scaling exponent $\zeta(m)$, when

$$S_m = \langle|\delta y_\tau|^m\rangle \sim \tau^{\zeta(m)} \quad (12)$$

whereas the PSD measures $\zeta(2)$ only (e.g., Marsch & Tu 1997; Horbury & Balogh 1997). We anticipate scaling for the data sets considered here, given the indication of a "$1/f$" range in the PSDs in Figure 1, however, power spectra alone cannot distinguish between fractal and multifractal behavior (Chapman et al. 2005). From Equation (12), the scaling exponents $\zeta(m)$ are given quantitatively by the slopes of the GSFs. Generally for perfectly self-affine processes, $\zeta(m)$ can be described by a linear equation $\zeta(m) = Hm$, where $H$ is the Hurst exponent. Each successful computation of a GSF at increasingly high-order yields additional information about the nature of the PDF of fluctuations. For practical applications of the GSF analysis to a broad range of data sets, see for example: MHD turbulence simulations, Merrifield et al. (2005, 2006, 2007); solar wind turbulence, Horbury & Balogh (1997); Hnat et al. (2005); Chapman & Hnat (2007); Nicol et al. (2008); geomagnetic indices, Hnat et al. (2003); laboratory plasma turbulence, Budaev et al. (2006); Dewhurst et al. (2008); Hnat et al. (2008) and references therein. We now apply these methods to the observations. Figure 8 shows the GSFs up to $m = 4$ for $\delta v_{\|}$, $\delta v_{\perp}$, $\delta b_{\|}$, and $\delta b_{\perp}$ for fast and slow solar wind at solar minimum. The series is differenced over $\tau = n \times 640$ s for $n = 1$ to 160, that is for a range covering 10–1706 minutes ($\sim$28 hr). The finite length of the data sets considered means that the statistics calculated for any given single ensemble can in principle be affected by the presence of large outliers, which are insufficiently numerous to be fully sampled. We

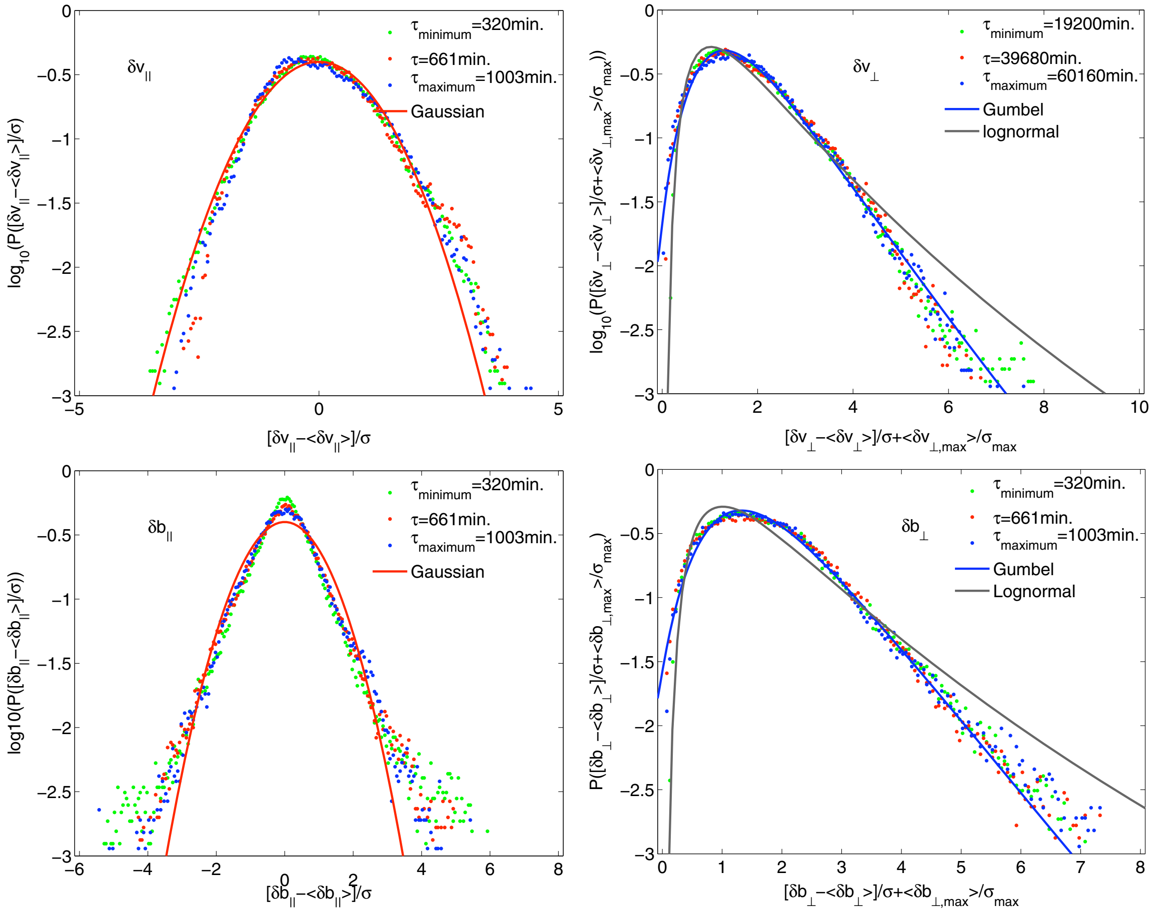


**Figure 5.** Parallel and perpendicular velocity and magnetic field fluctuations $\delta v_{\|,\perp}$ and $\delta b_{\|,\perp}$ in the fast solar wind at solar minimum for the "$1/f$" range. For clarity, plots for only three representative values of $\tau$ are shown for each component, whereas the fitted curves are computed using all the $\tau$ intervals between 320 and 1003 minutes. The left panels show a Gaussian fit to the normalized PDF curves for both $\delta v_{\|}$ (upper) and $\delta b_{\|}$ (lower) using semilog $y$-axes. The right panels show the normalized curves $\delta v_{\perp}$ (upper) and $\delta b_{\perp}$ (lower) fitted with two different distributions Gumbel (blue); and lognormal (gray) on semilog $y$-axis. For the perpendicular components, the renormalization with $\mu$ means that the PDFs are shifted so that they are centered on zero, however, the lognormal distribution can only have positive arguments. It is therefore necessary to shift the PDFs by $\langle \delta v_{\perp,\max}\rangle/\sigma_{\max}$.

(A color version of this figure is available in the online journal.)

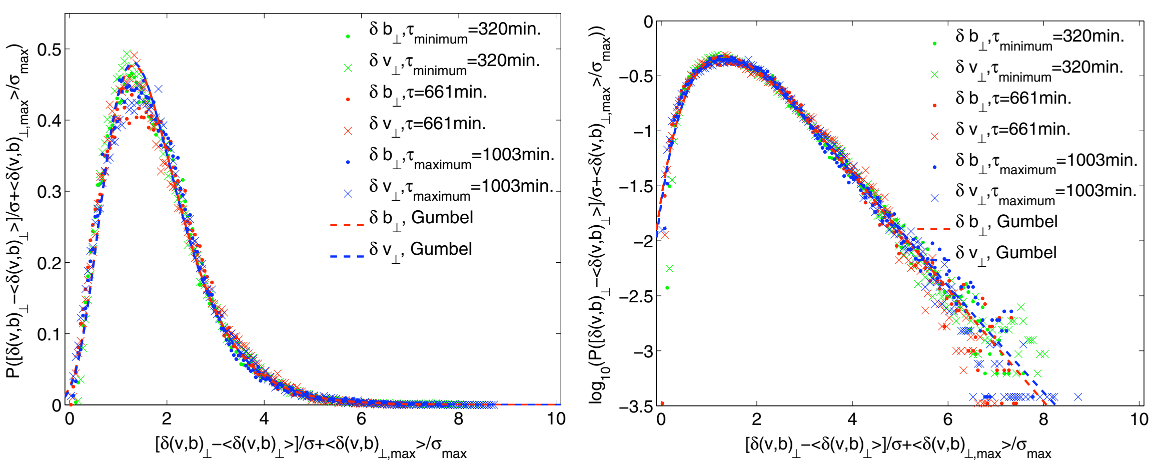


**Figure 6.** Perpendicular magnetic field fluctuations $\delta b_{\perp}$ ("·") and $\delta v_{\perp}$ ("×") in the fast solar wind at solar minimum for the "$1/f$" range. The Gumbel distribution is used to fit the normalized curves for $\delta b_{\perp}$ (red) and $\delta v_{\perp}$ (blue). Only three representative values of $\tau$ are shown for each component, whereas the fitted curves are computed using all the $\tau$ intervals. The left panel shows the PDFs on the linear axis, whereas the right panel shows the normalized curves on a semilog $y$-axis.

(A color version of this figure is available in the online journal.)

check that this does not bias our results via the method of Kiyani et al. (2006; see also Kiyani et al. 2007), which by subtracting outliers verifies whether calculated exponents are robust against statistical fluctuations in the outliers. The raw and 0.4% conditioned GSFs are shown for comparison in Figure 8. For the low-order moments that we consider here,

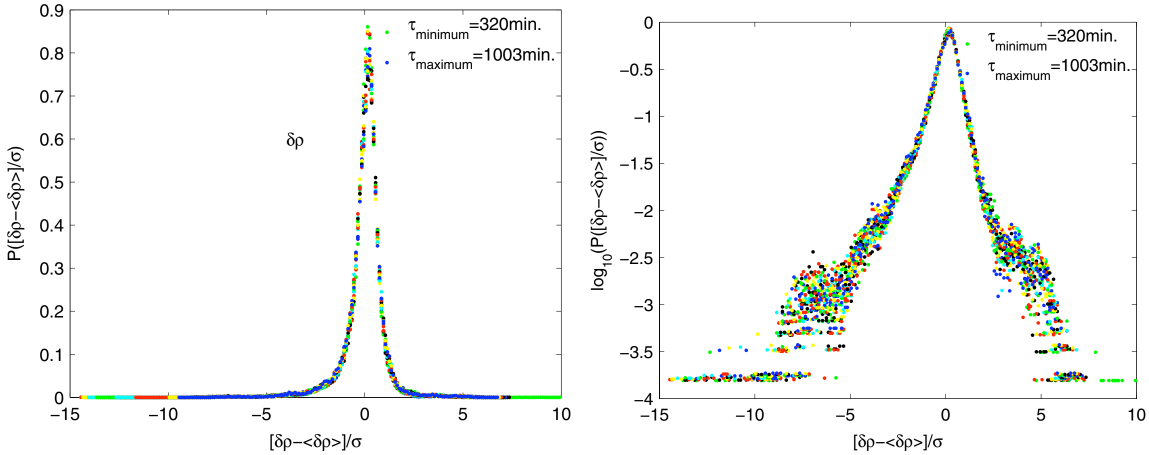


**Figure 7.** Ion density fluctuations $\delta\rho$ in the fast solar wind at solar minimum for the "$1/f$" range. The left panel shows the PDFs of raw fluctuations sampled across intervals $\tau$ between 320 and 1003 minutes normalized using Equation (8). The right panel shows the normalized curves on a semilog $y$-axis.

(A color version of this figure is available in the online journal.)

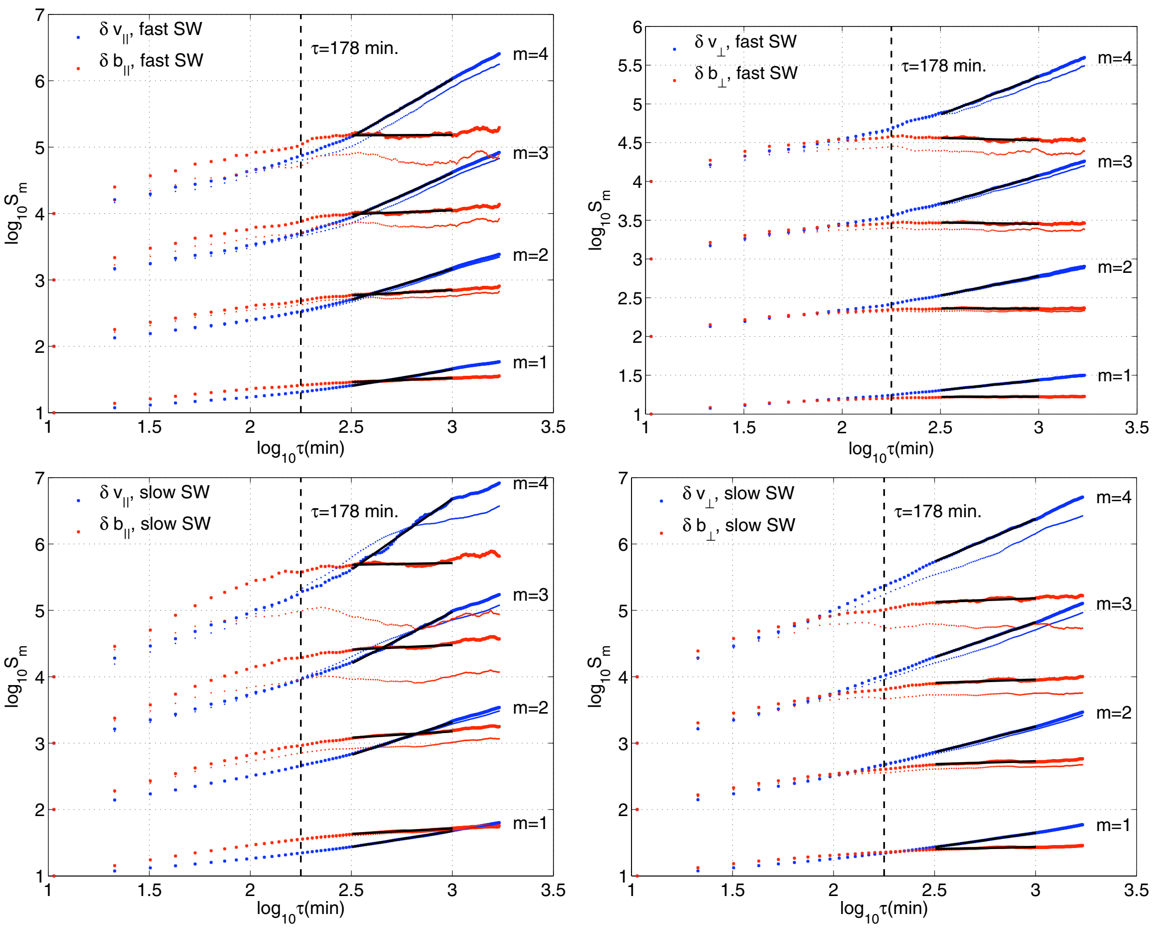


**Figure 8.** Comparison of scaling properties of fluctuations in the fast solar wind (upper) and in the slow solar wind (lower) at solar minimum in 2007. Generalized structure functions $S_m$ are plotted on log–log axes vs. sampling interval $\tau$ for $\tau = 10$–1706 minutes and $m = 1$–4. Left panels show parallel components of fluctuations in velocity (blue) and magnetic field (red); right panels show corresponding perpendicular components. The raw data are shown by "$\cdot p$," whereas "\boldmath $\cdot p$" denote data which has been conditioned by 0.4% (the difference in these curves quantifies finite size effects). Linear regression fits to the "$1/f$" range over $\tau = 320$—1002 minutes are shown. The transition from the IR to the "$1/f$" range occurs at ~178 minutes and is shown by the dashed line.

(A color version of this figure is available in the online journal.)

we see that the difference is small, so that the finite length of our data sets does not significantly affect our conclusions. The raw data are used for the plots of the probability densities of the fluctuations in Section 3. Figure 8 is consistent with the results shown previously, namely that $\boldsymbol{v}$ and $\boldsymbol{B}$ fluctuations exhibit very different behavior in the "$1/f$" range, which corresponds to large $\tau$ intervals. A simple self-affine noise process with PSD $\sim 1/f^{\alpha}$, $\alpha \sim 1$ would on such a plot have $\zeta(2) \to 0$ since $\alpha = 1 + \zeta(2)$. If the process is fractal then $\zeta(m) = \alpha m \to 0$ for all $m$. Thus we see that at $\tau > 178$ min.,

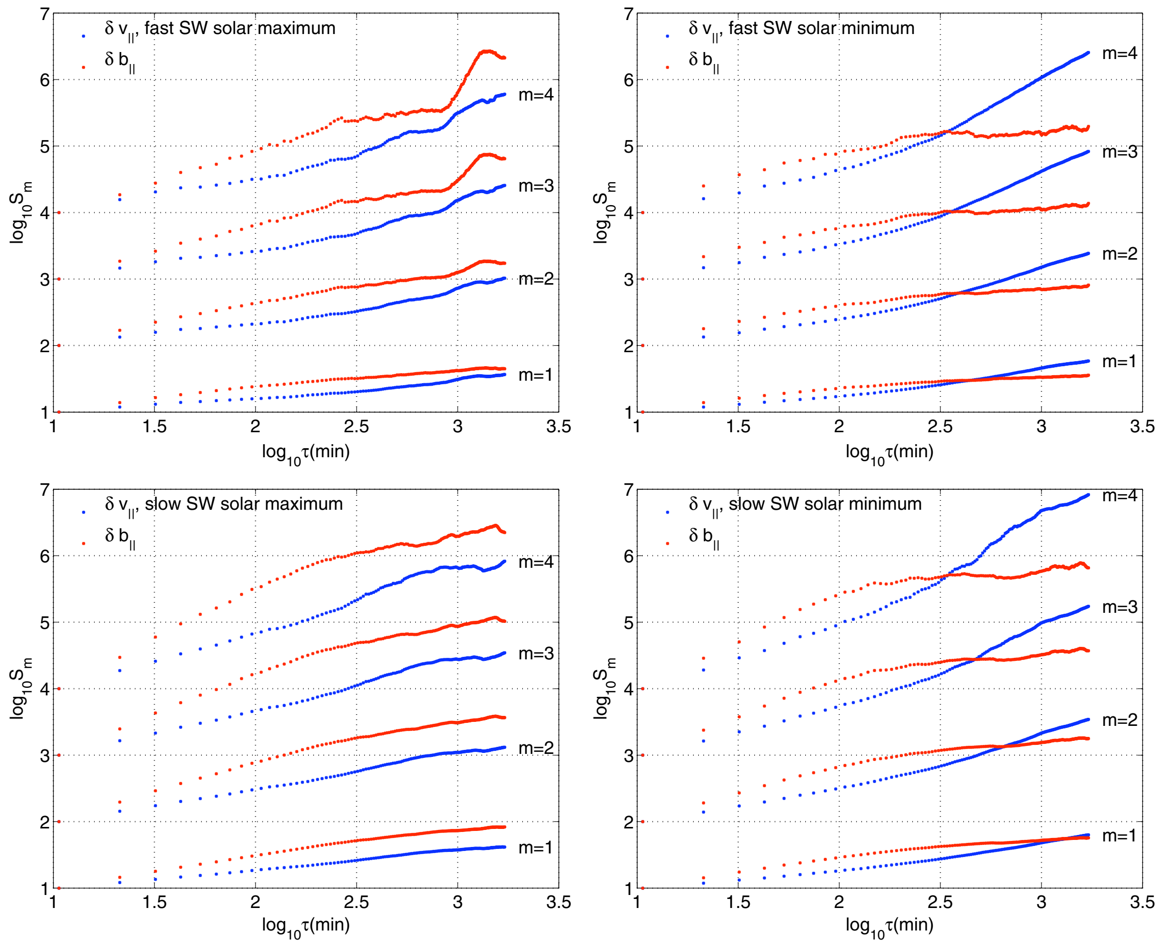


**Figure 9.** Comparison of scaling properties of parallel fluctuations between fast (upper) and slow (lower) solar wind at solar maximum (left) in 2000 and solar minimum (right) in 2007. Generalized structure functions $S_m$ are plotted on log–log axes vs. sampling interval $\tau$ for $\tau$ = 10–1706 minutes and $m$ = 1–4. Parallel components of fluctuations in velocity (blue) and magnetic field (red) are shown.

(A color version of this figure is available in the online journal.)

the GSFs for $\delta b_{\parallel,\perp}$ "flatten" in the $\sim 1/f$ range, consistent with previously reported results based on the PSD (Matthaeus & Goldstein 1986; Matthaeus et al. 2007). The $\delta v_{\parallel,\perp}$ GSFs on the contrary steepen at $\tau > 178$ minutes, showing a scaling process and exponents distinct from those of $\delta b_{\parallel,\perp}$. These are closer to a value of $\zeta(2) \sim 1$, which, again for a simple noise process, is consistent with PSD $\sim 1/f^2$. This is what we have seen in the PDF curve renormalization of the previous section: the $\delta b_{\parallel,\perp}$ raw PDFs were close to the renormalized PDFs, since the normalization is with respect to the first two moments $S_1$ and $S_2$, which for $\delta b_{\parallel,\perp}$ vary weakly as a function of scale $\tau$. Equation (12) tells one that the scaling behavior of the process is contained in the $\zeta(m)$ exponents, given by the slopes of the GSFs. We obtain these values by linear fits to the log–log GSF plots.

Whilst these results confirm the "$1/f$" scaling of fluctuations in $\boldsymbol{B}$ on long timescales, reported previously by for example Matthaeus & Goldstein (1986), they also highlight the distinct scaling of $\boldsymbol{v}$, which we will investigate next. These GSF plots of fluctuations oriented with respect to the background field also clearly show the crossover between the IR and "$1/f$" for fast and slow solar wind. The "$1/f$" range is much shorter in the slow streams, consistent with previous observations (e.g., Bruno & Carbone 2005; Horbury et al. 2005). The minimum value of $\tau$ that we will use for the following analysis can be seen to be greater than the breakpoint $\tau$ for both velocity and magnetic field fluctuations. It is also interesting to note that although the PDFs of $\delta v_\perp$ and $\delta b_\perp$ in the fast quiet solar wind show the same functional form (Figure 6), their GSF scalings are very different. This may suggest that the fluctuations $\delta v_\perp$ and $\delta b_\perp$ originate in a common coronal source, but their subsequent development differs in the evolving and expanding solar wind.

Figures 9 and 10 compare the GSFs for fast and slow solar wind streams at solar maximum (2000) and minimum (2007); for clarity only the 0.4% conditioned results are shown.

Figures 9 and 10 suggest that the scaling properties of $\delta v_\perp$ and $\delta b_\perp$ do not change with solar cycle in fast solar wind. However $\delta v_\parallel$ does, while the solar cycle dependence of $\delta b_\parallel$ is indeterminate. The divergences at $\tau \gtrsim 10^3$ minutes in the fast solar wind at solar maximum may be due to finite size effects: the data set for solar maximum is shorter than for solar minimum, because there are fewer long continuous time periods of fast solar wind. Figures 9 and 10 also show that the scaling properties of all four fluctuating quantities in the slow solar wind differ between solar maximum and minimum, due to different scaling exponents or a different breakpoint location.

Let us summarize our conclusions from the GSF analysis.

1. The breakpoints between the scaling properties measured by GSF analysis are different between fast and slow solar wind streams, and between periods of maximum and minimum solar activity.

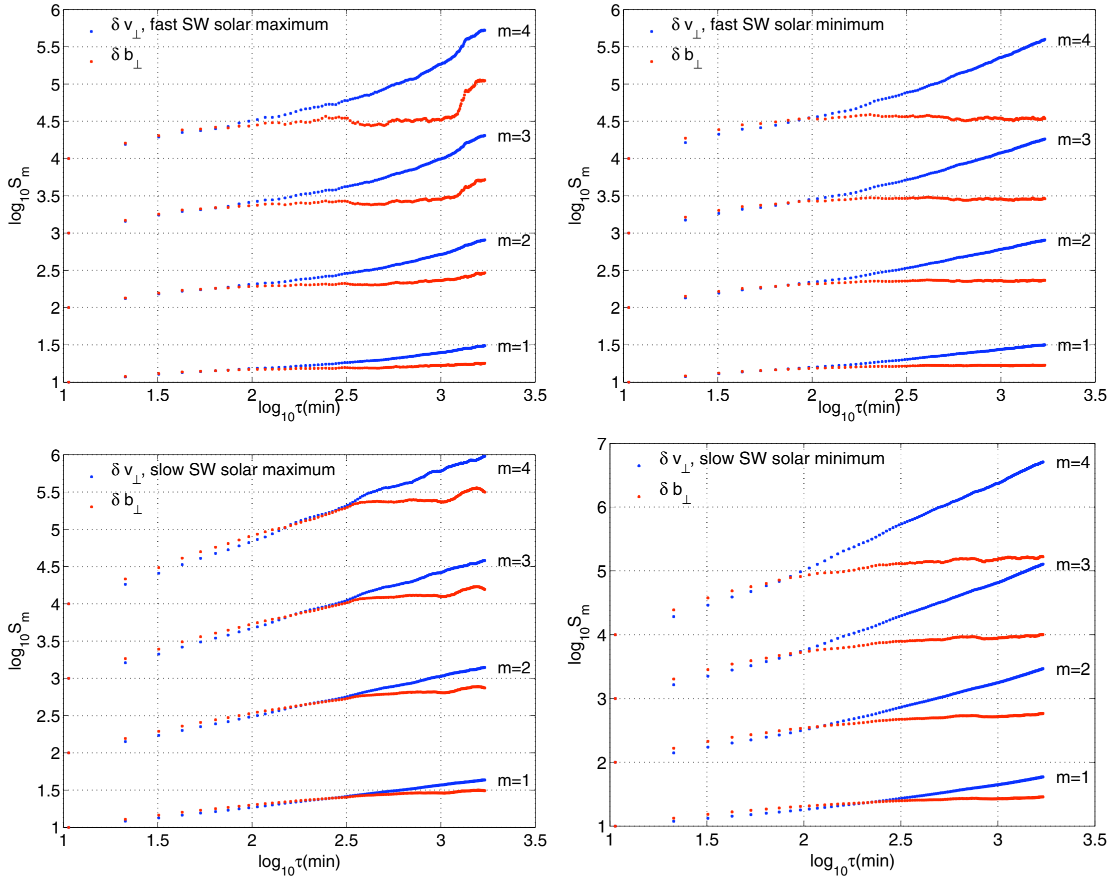


**Figure 10.** Comparison of scaling properties of perpendicular fluctuations between fast (upper) and slow (lower) solar wind at solar maximum (left) in 2000 and solar minimum (right) in 2007. Generalized structure functions $S_m$ are plotted on log–log axes vs. sampling interval $\tau$ for $\tau$ = 10–1706 minutes and $m$ = 1–4. Perpendicular components of fluctuations in velocity (blue) and magnetic field (red) are shown.

(A color version of this figure is available in the online journal.)

2. These breakpoints do not necessarily coincide with the breakpoint between IR and "$1/f$" ranges inferred from spectral analysis, however as mentioned earlier, it is difficult to extract precise quantitative information from the power spectra plots.
3. The IR extends to longer timescales in slow solar wind streams and at periods of maximum solar activity (e.g., Horbury et al. 2005), this is particularly clear in the GSFs of the perpendicular components in Figure 10.
4. The IR remains relatively robust for both slow and fast solar wind streams and is independent of solar cycle. This is to be expected if the IR is established by a turbulent cascade within the evolving expanding solar wind, rather than by initial conditions in the corona.
5. Intriguingly, $\delta v_\perp$ and $\delta b_\perp$ have the same behavior in the "$1/f$" range for fast solar wind at both solar maximum and minimum. Their scaling looks similar for the slow solar wind, but the breakpoint moves to longer timescales at solar maximum.
6. All four quantities vary between fast and slow solar wind and solar minimum and maximum.

## 5. QUANTIFYING THE SCALING EXPONENTS

Let us now quantify the observed scaling by measuring the slopes of the GSFs to obtain estimates of the values of the scaling exponents, $\zeta(m)$; the robustness of the scaling will also be tested. In principle, values for $\zeta(m)$ are obtained from the gradients of the log–log plots of $S_m$ versus $\tau$. In practice, these are affected by the fact that both the length of the data set and the range of $\tau$ over which we see scaling are finite. As a preliminary, therefore, we outline a method to optimize this process to obtain a good estimate of the exponents.

### 5.1. p-*model and Brownian Walk Test Time Series*

We begin by considering a simple self-affine process where $S_m \sim \tau^{\zeta(m)}$, $\zeta(m) = Hm$. A fractal (self-affine) time series will in principle always give the same value of $H$ if computed from any region, or range of values, of the PDF of fluctuations (differences) sampled across a timescale $\tau$. We seek to choose the most statistically significant subset, and we do this by recomputing $H$ for different regions of the PDF; if the process is fractal, we expect to find the same $H$. To probe the full range of behavior in the PDF, including any extended tails, we need to test for convergence to a single value of $H$ for a wide dynamic range of the PDF, for example $\sim 20\sigma$. The largest values explored by the PDF of the data are the least well sampled statistically. It follows that if we successively remove these outliers, we should see, for a fractal time series, rapid convergence to a constant $H$ value. This is shown in Figure 11 (top panel) for a Brownian walk, see also Kiyani et al. (2007). The scaling for a Brownian walk with normally distributed steps demonstrates the expected behavior for a fractal process without heavy tails. On the other hand, a multifractal process does not return a single constant value of $H$ as one changes the range of values over which $H$ is computed; this can be seen for the multifractal

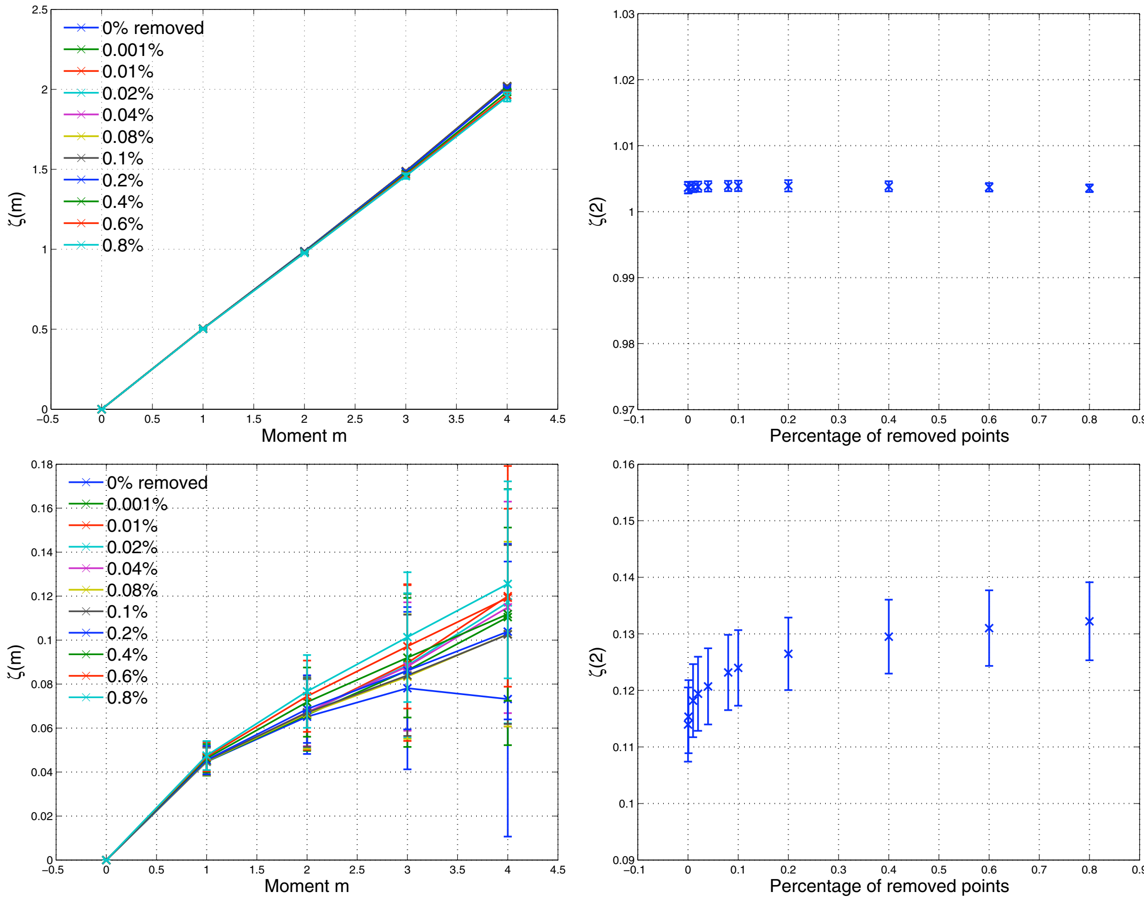


**Figure 11.** Finite size effects on fractal and multifractal processes. The left-hand panels show the scaling exponents $\zeta(m)$ plotted as a function of moment $m = 1$–6 for different percentages of removed points. The right-hand panels show $\zeta(2)$ plotted against the percentage of removed points. The two top panels show the scaling for a Brownian walk, which has normally distributed steps; and the two bottom panels are the results for a multifractal p-model (Kiyani et al. 2007).

(A color version of this figure is available in the online journal.)

$p$-process (Meneveau & Sreenivasan 1987) in the lower panel of Figure 11. A plot of the value of the exponent (here $\zeta(2)$) as we successively remove outliers then can distinguish fractal and multifractal processes. For processes that are fractal, it also provides a more precise determination of the single exponent $H$ that characterizes the time series. The errors are obtained by combining the least squares error in the $\zeta(m)$ value fitted across the full range, with the standard deviation of the $\zeta(m)$ values fitted across runs of data points that have varying lengths, starting with a minimum length of about half the total fitting range length, centered on the middle of the full fitting range. This method is applied for all the exponent statistics throughout this paper.

### 5.2. *Fast Quiet Solar Wind Scaling*

We now quantify the scaling exponents of $\delta v_{\parallel}$ and $\delta v_{\perp}$ fluctuations in the fast solar wind at solar minimum. The corresponding GSFs are plotted in the top right panels of Figures 9 and 10. We plot the exponents $\zeta(m)$, which are the gradients of the fitted power laws, from $\tau = 320$ to 1002 minutes in Figure 12. In the lower panels, we show how the value of $\zeta(2)$ changes as outliers are successively removed. Comparing with Figure 11, we infer that $\delta v_{\parallel}$ is fractal within errors and $\delta v_{\perp}$ is only very weakly multifractal (almost monofractal). For the exponents, we obtain $\zeta_{\parallel}(2)$ close to 1, suggestive of near Gaussian behavior and (if the relation $\alpha = 1 + \zeta(2)$ holds) a PSD $\sim 1/f^2$. In contrast, the exponent for perpendicular fluctuations $\zeta_{\perp}(2)$ is close to 0.5, implying a PSD $\sim 1/f^{3/2}$. Figure 13 compares the scaling exponents $\zeta(2)$ for $\delta v_{\parallel}$ and $\delta v_{\perp}$ in fast and slow solar wind streams at solar minimum. The corresponding GSFs are plotted in the right-hand pairs of panels in Figures 9 and 10. Fluctuations of $\delta v_{\parallel}$ in the slow solar wind appear more strongly multifractal than in the fast wind. For $\delta v_{\perp}$ the slow solar wind displays a much higher exponent value for slow ($\zeta(2) \sim 0.8$) than for fast ($\zeta(2) \sim 0.5$) streams, reflecting the intrinsic differences between the fast and slow solar wind, and the coronal plasma conditions and magnetic field configuration at their origin. To summarize the observed results:

1. Analysis of the scaling exponents reveals fractal or weakly multifractal (very close to monofractal) scaling in the fluctuations of velocity components in the fast solar wind, with very different values for $\delta v_{\parallel}$ ($\zeta(2) \sim 0.95$) and $\delta v_{\perp}$ ($\zeta(2) \sim 0.5$) at solar minimum.
2. In the slow solar wind at solar minimum, the scaling exponent $\zeta(2)$ of $\delta v_{\perp}$ nearly doubles from ∼0.5 to ∼0.8. In contrast, the scaling of $\delta v_{\parallel}$ remains quantitatively similar to its value in the fast wind (Figure 13), i.e., $\zeta(2) \sim 0.95$ but has a less well-defined monofractal character.
3. If we assume a regime in which the PSD $f^{-\alpha}$ scaling exponent $\alpha$ is related to $\zeta(2)$ by $\alpha = 1 + \zeta(2)$, then we obtain for the fast quiet solar wind: $\alpha \sim 1$ for $\delta b_{\parallel,\perp}$ (as

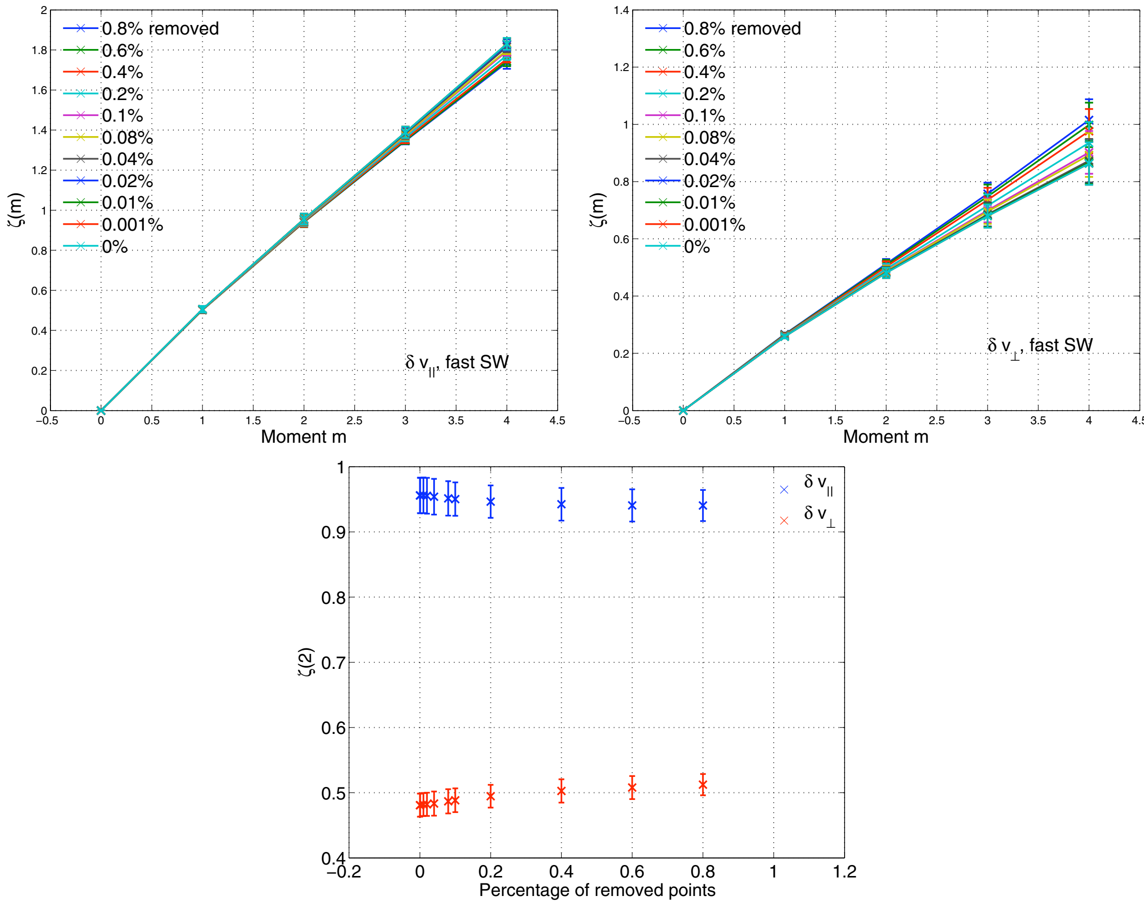


**Figure 12.** Scaling properties of fluctuations $\delta v_\parallel$ and $\delta v_\perp$ in the "$1/f$" range, $\tau = 320$–1002 minutes, in the fast solar wind at solar minimum. The upper panels show the $\zeta(m)$ exponents plotted as a function of moment $m = 1$–4 for different percentages of removed points for $\delta v_\parallel$ (left) and $\delta v_\perp$ (right). The bottom panel shows $\zeta(2)$ plotted against the percentage of removed points for $\delta v_\parallel$ (blue, upper) and $\delta v_\perp$ (red, lower).

(A color version of this figure is available in the online journal.)

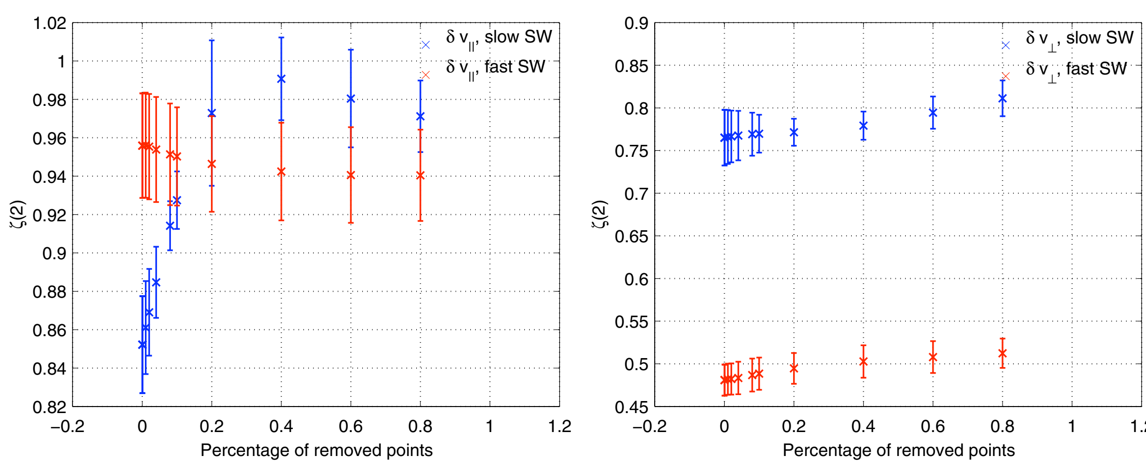


**Figure 13.** Comparisons of $\zeta(2)$ at solar minimum in the "$1/f$" range as a function of the percentage of removed points for fast (red) and slow (blue) solar wind streams for $\delta v_\parallel$ (left) and $\delta v_\perp$ (right). The slow solar wind scaling appears to be more strongly multifractal.

(A color version of this figure is available in the online journal.)

expected from Figure 1), $\alpha \sim 2$ for $\delta v_\parallel$ and $\alpha \sim 1.5$ for $\delta v_\perp$.

## 6. CONCLUSIONS

We have examined the scaling of the parallel and perpendicular velocity and magnetic field fluctuations measured in the solar wind at ∼1 AU by *ACE*, which we have decomposed with respect to a locally averaged background magnetic field. Power spectra, GSFs, and PDF collapse have been used to qualify and quantify the nature of the observed scaling in the low-frequency "$1/f$" range. Slow and fast solar wind streams have been compared at both solar maximum in 2000 and solar minimum in 2007. The slow solar wind is found to be more multifractal and complex than the fast solar wind. In contrast, self-affine scaling is observed for the velocity fluctuations in the fast solar wind at solar minimum. This suggests that indeed the "$1/f$" range is not simply an in situ turbulent cascade, but rather carries the signature of scaling processes other than in situ turbulence.

1. The magnetic field fluctuations display a flattening of the GSFs for $\tau \geqslant 178$ minutes and a spectral index $\sim 1$, consistent with $\sim 1/f$ behavior found previously (Matthaeus & Goldstein 1986; Matthaeus et al. 2007).
2. The velocity fluctuations show strong anisotropy, with scaling behavior distinct from that of the $\boldsymbol{B}$ field and characterized by steepening of the GSFs in the "$1/f$" range (Figure 8) consistent with $\sim 1/f^{\alpha}$, $\alpha \neq 1$.

For the fast quiet solar wind:

1. $\delta v_{\parallel}$ and $\delta v_{\perp}$ have different scaling exponents: $\delta v_{\parallel}$ exhibits fractal scaling with $\zeta(2) \sim 0.95 \pm 0.02$ whereas $\delta v_{\perp}$ is weakly multifractal with $\zeta(2) \sim 0.49 \pm 0.03$ (Figure 12). The PDFs for these quantities also rescale relatively well. The PDF of $\delta v_{\parallel}$ is close to Gaussian, whereas $\delta b_{\parallel}$ is nearly symmetric and has stretched exponential tails, consistent with a multiplicative process.
2. The rescaled PDFs for $\delta v_{\perp}$ and $\delta b_{\perp}$ can be fitted with the same distribution function, which is close to gamma or inverse Gumbel (see Figure 6). However, their scaling exponents revealed by GSFs differ substantially (see Figure 10).
3. These observations are consistent with a common coronal source for the fluctuations but a different spatiotemporal evolution out to 1 AU. The functional form of the PDF then constrains the mechanism that generates the fluctuations at the corona, gamma having points of contact with turbulence in confined plasmas (see, for example, Graves et al. 2005; Labit et al. 2007, and references therein) and Gumbel, as an extremal process.

We also note that the breakpoint between the IR and "$1/f$" ranges differs between fast and slow solar wind streams and between periods of maximum and minimum solar activity.

1. The IR extends to longer timescales in slow solar wind streams and at periods of maximum solar activity.
2. The values of the IR scaling exponents remain unaffected by changes in the solar cycle (Figures 9 and 10), consistent with locally generated turbulence.

Our results clearly show very different behavior between the magnetic and velocity fluctuations in the "$1/f$" range. The fractal nature of $\delta v_{\parallel}$ points to distinct physical processes in the corona, and to their mapping out into the solar wind. Further work would involve relating the fractal scaling observed at $\sim 1$ AU with fractal stirring of magnetic footpoints in the corona. The different scaling observed in $\delta v_{\perp}$ points to different dynamics perpendicular to the background field (field line interactions?) with a possible common coronal origin for the $\delta v_{\perp}$ and $\delta b_{\perp}$ fluctuations in fast quiet solar wind.

R.N. acknowledges the STFC and UKAEA Culham for financial support and R. P. Lepping and the ACE team for data provision.

## REFERENCES


Bavassano, B., Bruno, R., & D'Amicis, R. 2005, Ann. Geophys., 23, 1025
Bavassano, B., Dobrowolny, M., Mariani, F., & Ness, N. F. 1982, J. Geophys. Res., 87, 3617
Bruno, R., & Carbone, V. 2005, Living Rev. Solar Phys., 2, 4
Bruno, R., Carbone, V., Primavera, L., Malara, F., Sorriso-Valvo, L., Bavassano, B., & Veltri, P. 2004, Ann. Geophys., 22, 3751
Budaev, V. P., Takamura, S., Ohno, N., & Masuzaki, S. 2006, Nucl. Fusion, 46, 181
Burlaga, L. F., & Forman, M. A. 2002, J. Geophys. Res., 107, 1403
Chapman, S. C., & Hnat, B. 2007, Geophys. Res. Lett., 34, 17103
Chapman, S. C., Hnat, B., Rowlands, G., & Watkins, N. W. 2005, Nonlinear Process. Geophys., 12, 767
Dendy, R. O., & Chapman, S. C. 2006, Plasma Phys. Control. Fusion, 48, B313
Dewhurst, J. M., Hnat, B., Ohno, N., Dendy, R. O., Masuzaki, S., Morisaki, T., & Komori, A. 2008, Plasma Phys. Control. Fusion, 50, 095013
Dudson, B. D., Dendy, R. O., Kirk, A., Meyer, H., & Counsell, G. F. 2005, Plasma Phys. Control. Fusion, 47, 885
Feynman, J., & Ruzmaikin, A. 1994, J. Geophys. Res., 99, 17645
Frisch, U., & Sornette, D. 1997, J. Physique I, 7, 1155
Galtier, S., Nazarenko, S. V., Newell, A. C., & Pouquet, A. 2000, J. Plasma Phys., 63, 447
Goldreich, P., & Sridhar, S. 1995, ApJ, 438, 763
Gosling, J. T., Asbridge, J. R., Bame, S. J., Feldman, W. C., Borrini, G., & Hansen, R. T. 1981, J. Geophys. Res., 86, 5438
Graves, J. P., Dendy, R. O., Hopcraft, K. I., & Jakeman, E. 2002, Phys. Plasmas, 9, 1596
Graves, J. P., Horacek, J., Pitts, R. A., & Hopcraft, K. I. 2005, Plasma Phys. Control. Fusion, 47, L1
Greenhough, J., Birch, P. C., Chapman, S. C., & Rowlands, G. 2002, Physica A, 316, 615
Greenhough, J., Chapman, S. C., Chaty, S., Dendy, R. O., & Rowlands, G. 2002, A&A, 385, 693
Hnat, B., Chapman, S. C., & Rowlands, G. 2005, J. Geophys. Res., 110, 8206
Hnat, B., Chapman, S. C., Rowlands, G., Watkins, N. W., & Freeman, M. P. 2003, Geophys. Res. Lett., 30, 220000
Hnat, B., Dudson, B. D., Dendy, R. O., Counsell, G. F., & Kirk, A. the MAST Team 2008, Nucl. Fusion, 48, 085009
Horbury, T. S., & Balogh, A. 1997, Nonlinear Process. Geophys., 4, 185
Horbury, T. S., Balogh, A., Forsyth, R. J., & Smith, E. J. 1995, Ann. Geophys., 13, 105
Horbury, T. S., Balogh, A., Forsyth, R. J., & Smith, E. J. 1996, J. Geophys. Res., 101, 405
Horbury, T. S., Forman, M. A., & Oughton, S. 2005, Plasma Phys. Control. Fusion, 47, 703
Horbury, T. S., Forman, M.A., & Oughton, S. 2008, Phys. Rev. Lett., 101, 175005
Kiyani, K., Chapman, S. C., & Hnat, B. 2006, Phys. Rev. E, 74, 051122
Kiyani, K., Chapman, S. C., Hnat, B., & Nicol, R. M. 2007, Phys. Rev. Lett., 98, 211101
Krieger, A. S., Timothy, A. F., & Roelof, E. C. 1973, Sol. Phys., 29, 505
Labit, B., Furno, I., Fasoli, A., Diallo, A., Müller, S. H., Plyushchev, G., Podestà, M., & Poli, F. M. 2007, Phys. Rev. Lett., 98, 255002
Marsch, E., & Tu, C.-Y. 1990a, J. Geophys. Res., 95, 8211
Marsch, E., & Tu, C.-Y. 1990b, J. Geophys. Res., 95, 11945
Marsch, E., & Tu, C.-Y. 1997, Nonlinear Process. Geophys., 4, 101
Matthaeus, W. H., Breech, B., Dmitruk, P., Bemporad, A., Poletto, G., Velli, M., & Romoli, M. 2007, ApJ, 657, L121
Matthaeus, W. H., & Goldstein, M. L. 1986, Phys. Rev. Lett., 57, 495
Matthaeus, W. H., Goldstein, M. L., & Roberts, D. A. 1990, J. Geophys. Res., 95, 20673
McComas, D. J., Bame, S. J., Barker, P., Feldman, W. C., Phillips, J. L., Riley, P., & Griffee, J. W. 1998, Space Sci. Rev., 86, 563
Meneveau, C., & Sreenivasan, K. R. 1987, Phys. Rev. Lett., 59, 1424
Merrifield, J. A., Arber, T. D., Chapman, S. C., & Dendy, R. O. 2006, Phys. Plasmas, 13, 012305
Merrifield, J. A., Chapman, S. C., & Dendy, R. O. 2007, Phys. Plasmas, 14, 012301
Merrifield, J. A., Müller, W.-C., Chapman, S. C., & Dendy, R. O. 2005, Phys. Plasmas, 12, 022301
Ng, C. S., & Bhattacharjee, A. 1997, Phys. Plasmas, 4, 605
Nicol, R. M., Chapman, S. C., & Dendy, R. O. 2008, ApJ, 679, 862
Oughton, S., Priest, E. R., & Matthaeus, W. H. 1994, J. Fluid Mech., 280, 95
Padhye, N. S., Smith, C. W., & Matthaeus, W. H. 2001, J. Geophys. Res., 106, 18635
Parker, E. N. 1958, ApJ, 128, 664
Ruzmaikin, A., Lyannaya, I. P., Styashkin, V. A., & Eroshenko, E. 1993, J. Geophys. Res., 98, 13303
Shebalin, J. V., Matthaeus, W. H., & Montgomery, D. 1983, J. Plasma Phys., 29, 525

Smith, C. W., L'Heureux, J., Ness, N. F., Acuña, M. H., Burlaga, L. F., & Scheifele, J. 1998, Space Sci. Rev., 86, 613
Sornette, D. 2004, Critical Phenomena in Natural Sciences: Chaos, Fractals, Selforganization and Disorder: Concepts and Tools, Springer Series in Synergetics, ed. D. Sornette (2nd ed.; Heidelberg: Springer)
Sorriso-Valvo, L., Carbone, V., & Bruno, R. 2004, Europhys. Lett., 67, 504
Sorriso-Valvo, L., et al. 2007, Phys. Rev. Lett., 99, 115001
Sridhar, S., & Goldreich, P. 1994, ApJ, 432, 612
Stone, E. C., Frandsen, A. M., Mewaldt, R. A., Christian, E. R., Margolies, D., Ormes, J. F., & Snow, F. 1998, Space Sci. Rev., 86, 1
Taylor, G. I. 1938, Proc. R. Soc. Lond. A, 164, 476
Wadsworth, H. M. 1997, Handbook of Statistical Methods for Engineers and Scientists ed. H. M. Wadsworth (2nd ed.; New York: McGraw-Hill)